

Fig. 1 *Manduca sexta* wings exhibit pronounced deformations during flight, shown here at ventral stroke reversal (photo by Armin Hinterwirth). Note the torsional deformation of the wing facing the camera

wing beat frequencies, we are able to resolve flows and deformation patterns with high-speed digital videography.

This study uses robotically actuated wings from a large moth that flaps its wings at 25 Hz. Due to the technological challenges of multi-axis actuation at such high frequencies, and in contrast to prior studies using scaled robotic models of insect wings (e.g., S2003), we use a single axis rotation to yield natural deformations that reasonably well approximate wing kinematics observed in flight. We rely on natural changes in wing stiffness combined with exceptionally high temporal resolution digital particle image velocimetry to quantify the flow consequences of wing deformation.

2 Materials and methods

(Ennos 1988; Norberg 1972; Wootton 1981; Wootton 1992). For example, Ennos (1988) showed that favorable

camber is automatically generated during wing translation in both odonates and dipterans as a consequence of the structural support of wing veins. Dynamic deformation patterns may also be dominated by purely inertial and elastic processes, remaining largely independent of the pressure distribution resulting from aerodynamic forces. Recent results for robotically actuated wings of hawkmoth, *Manduca sexta*, show that these wings deform nearly identically in air as they do in a low-pressure helium-filled chamber (15% of air density; Combes and Daniel 2003). Thus, we can predict that the pattern of deformation one observes in these wings is somewhat decoupled from the pressure distribution to which wings are normally exposed.

Dynamically scaled robotic models (e.g., matched Reynolds and Strouhal numbers, reviewed by S2003) are powerful tools for unraveling the complex aerodynamic forces and flows associated with model wings moving with complex kinematics. However, such dynamically scaled models are limited as biological proxies because structural dynamics do not scale in the same manner as fluids. It is thus a significant challenge to fabricate a dynamically scaled airfoil that faithfully recreates the emergent deformation patterns observed in flying insects.

Robotically actuated natural wings in air (as in Combes and Daniel 2003) provide unique opportunities for examining the interaction between dynamic deformations and the emergent flow patterns (e.g., momentum flux and vorticity). In such cases, we avoid the challenge of scaling structural elastic and inertial forces with fluid forces. We deformations of a robotically actuated sample wing unit (in face, however, the other technical challenge of providing kinematics at biologically relevant frequencies and amplitudes while measuring flows with very high temporal resolution. For large flying insects with relatively slow bat plate that best fit the deformed wing surface at each

2.1 Overview

We measured the flexural stiffness and induced flow fields in the 3 ipsilateral wing pairs of *M. sexta* each in both a fresh state and dry state. Wings extracted from freshly enclosed moths are more flexible than those allowed to dry and stiffen over time, permitting us to examine the consequences of wing stiffness to the flow field induced by their motion. Wings that undergo desiccation also lose mass, however, so we controlled for mass by applying spray paint to the dry wings until they regained their original weight. To quantify the overall difference in stiffness between fresh wings and dry wings, we used a proxy measurement of spanwise flexural stiffness, calculated using an applied ventral force and resulting wing deflection. Although the wings of insects have inhomogeneous, anisotropic distributions of flexural stiffness that differ not only in their spanwise-chordwise directions but also in their ventral-dorsal loading (Combes and Daniel 2003a, b), we did not focus on the details of wing structural properties in this study. Each wing pair was robotically actuated at its natural wingbeat frequency of 25 Hz, and we employed digital particle image velocimetry (PIV) to explore the consequences of wing stiffness to the emergent fluid dynamics at the ventral stroke reversal. We computed a representative velocity vector, the mean advective flow, for each flow field and used it to make general comparisons between the induced flows of different wing types.

consecutive time step throughout a complete ventral stroke reversal, and calculating the overall deviation of the wing surface from the flat plate.

Finally, we needed to rotate our robotic wing data into a biologically relevant configuration. Thus, we performed a principal components analysis on the wing trajectory of a hovering moth to determine its average stroke plane in global coordinates, onto which we mapped the stroke plan of our robotically actuated wing and rotated the PIV flow fields accordingly.

2.2 Flexible wing preparation

We extracted and prepared wings from six moths obtained from a captive-bred colony at the University of Washington. We selected individuals within 24 h of eclosion and cold-anesthetized them at 0 °C for 12–15 min. We removed each right forewing and hindwing pair at the thorax and fastened the wing bases adjacent to each other on the top edge of a 5 cm sheet metal mounting plate using cyanoacrylate glue cured with sodium bicarbonate. We mounted the forewing directly in front of the hindwing so that the trailing edge of the forewing slightly overlapped the leading edge of the hindwing, approximating their arrangement during natural flight. A small drop of cyanoacrylate glue applied between the dorsal side leading edge of the hindwing and the ventral side trailing edge of the forewing, approximately 2 cm distal to the hindwing base, adhered the two wings together where they overlapped. We weighed the mounted wing unit before proceeding with flexural stiffness measurements and PIV trials.

2.3 Dry wing preparation

Following each fresh wing PIV trial, we let the wing unit dry at room temperature for 12–24 h, during which time both lost mass and gained stiffness. After recording the weight of the dried wing unit, we applied a series of thin coats of evenly distributed spray enamel to both ventral and dorsal sides, periodically weighing the wing unit until we approximately reached its original weight when freshly mounted. Each of our three painted wing units deviated less than 1.5% from their original mass. We then repeated our flexural stiffness measurements and PIV trials on these dry, painted wing units.

2.4 Flexural stiffness measurements

We calculated the flexural stiffness of each wing unit by applying a series of point forces on the ventral wing surface, along the wingspan, and measuring the resulting wing displacements in photographed images in a method similar to that used by Combes and Daniel (2003a, b). We fastened

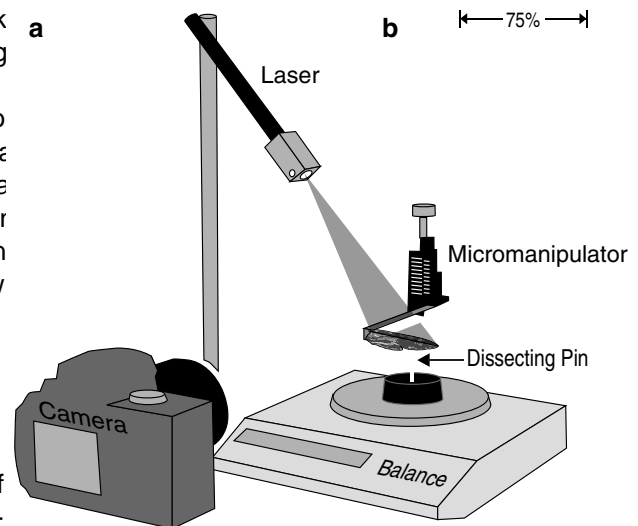


Fig. 2 Apparatus used to measure wing flexural stiffness. Wings were fixed to a micromanipulator and lowered onto the head of a dissection pin resting on a digital balance. A laser light sheet illuminated a spanwise line along the dorsal wing surface and a point force was applied via the pinhead at 75% wing span along the illuminated line. Wing deflection was captured in a photographed image for subsequent analysis

the wing unit, by the mounting plate, to an aluminum beam connected to a micromanipulator and positioned the wing above a dissection pin vertically mounted on a digital balance (Sartorius L610D; Fig. 2a). A 5 mm diameter quartz cylindrical rod was affixed to the front of a 100 mW red laser pointer (Pulsar P100, Wicked Lasers) to create a vertical light sheet that projected obliquely onto the dorsal wing surface. The light sheet illuminated a line running spanwise from the forewing base to the tip (Fig. 2b). Images were captured with a Nikon D40 digital camera and 60 mm micro lens positioned posterior to the wing and orthogonal to the laser light sheet. Using the micromanipulator we lowered the wing unit onto the pinhead at approximately 75% of the wingspan along the illuminated line (Fig. 2b). An initial photograph where its ventral surface only just made contact with the pinhead with no applied force measured by the scale. We then applied a series of point loads of varying magnitudes, photographing the deflected wing unit in each case and returning the wing to its unloaded state after each trial. We performed five to ten flexural stiffness trials on each wing unit. Lastly, we removed the wing unit and inserted a metric ruler at the same location, taking a final photograph for image calibration.

We analyzed each image of the deflected wing unit to determine its effective beam length and deflection. We used custom Matlab software (Hedrick 2008) to digitize our calibration and wing images. Digitizing the ruler

calibration image enabled us to convert image coordinate from pixels to meters. Beam length (l) was measured as the distance along the illuminated line from the base of the wing where it left the mounting plate to the point of applied force at the pinhead. Since the point of applied force was constant, deflection (δ) was measured as the vertical distance traveled by the micromanipulator from its initial reference location. We used these two measured values as the applied force (F), the product of mass reported on the balance readout and gravitational acceleration, to calculate the wing's overall spanwise flexural stiffness (EI) for each trial (Combes and Daniel 2003a, b):

$$EI \approx \frac{FL^3}{3\delta}$$

All wing deflection magnitudes in our trials were less than 5% of the effective beam length, as in Combes and Daniel (2003a).

2.5 Particle image velocimetry

By combining continuous laser light and high speed digital videography with short exposure times, we were able to compute induced flow fields at extremely high temporal resolution, exceeding 2,000 images/s at 0.6 megapixels per image.

Each wing unit was fastened to a brass rod attached to a pen motor from a Gould chart recorder and tapped sinusoidally around a dorsoventral axis of rotation at a frequency of 25 Hz and amplitude of 125 typical of hovering *M. sexta* (Willmott and Ellington 1997). The motor was mounted to a platform in the center of a glass chamber (42 cm × 27 cm × 31 cm; Fig. 3a). A 5 mm diameter quartz cylindrical rod was affixed to the front of a 200 mW, 532 nm continuous green laser pointer (Spyder I Mat PIV 1.6.1, an open-source toolbox for Matlab (Sveen GX, Wicked Lasers) to create a vertical light sheet projecting down the length of the chamber, parallel to the axis of wing rotation. The flapping wing intersected the light sheet at ventral stroke reversal, illuminating a chordwise wing section at 75% wingspan during supination (Fig. 3b). The laser rode on a mini optical rail (Newport), allowing us to position the light sheet at the proper spanwise location for each wing. We seeded the chamber with Lycopodium spores (mean diameter 300 nm) as tracer particles (as in Dickinson and Gotz 1996).

A Phantom v5.1 high speed digital camera (Vision Research) with a 50 mm Nikon lens imaged the induced flow patterns illuminated by the orthogonal laser light sheet. We used a camera frame rate of 2,100 frames/s, a shutter speed of 200 ms, and a lens aperture of 1.2 to capture images with a pixel resolution of 768 × 688. Both camera and motor were simultaneously controlled by a custom signal-generating Matlab program (Mathworks) via

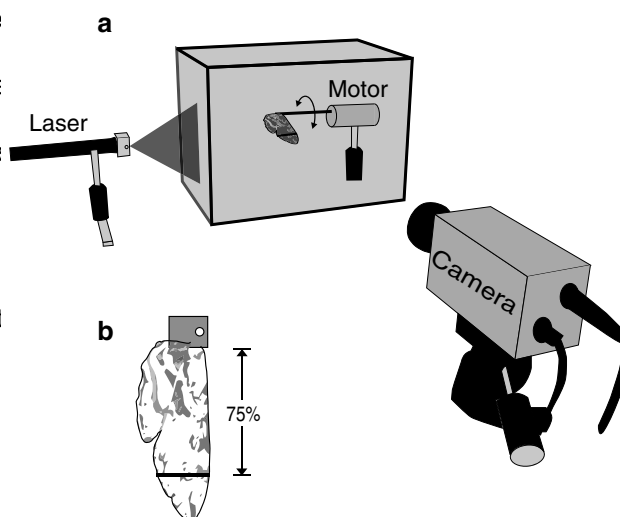


Fig. 3 Apparatus used to image induced flows around a robotically actuated moth wing for PIV analysis. A right ipsilateral wing pair was fixed to a motor within a glass chamber and oscillated at 25 Hz. A 200 mW continuous laser light sheet was projected down the center of the chamber, illuminating a chordwise wing section at 75% wingspan during ventral stroke reversal. The chamber was seeded with Lycopodium spores as tracer particles and flows were imaged at 2,100 frames/s with a high-speed digital camera

and were phase-locked at 84 images per wing stroke.

Prior to each trial we introduced a 5 s burst of compressed air into the chamber through a flexible hose to suspend a majority of the Lycopodium spores, then waited 10 s for the injected turbulence from the air hose to dissipate before beginning our trial. The wing unit was driven for 25 strokes (1 s total duration) for each trial, and we recorded the final 10 strokes for subsequent PIV analysis. Particle image velocimetry analysis was performed with MatPIV 1.6.1, an open-source toolbox for Matlab (Sveen GX, Wicked Lasers) to create a vertical light sheet projecting down the length of the chamber, parallel to the axis of wing rotation. The flapping wing intersected the light sheet at ventral stroke reversal, illuminating a chordwise wing section at 75% wingspan during supination (Fig. 3b). The laser rode on a mini optical rail (Newport), allowing us to position the light sheet at the proper spanwise location for each wing. We seeded the chamber with Lycopodium spores (mean diameter 300 nm) as tracer particles (as in Dickinson and Gotz 1996).

A Phantom v5.1 high speed digital camera (Vision Research) with a 50 mm Nikon lens imaged the induced flow patterns illuminated by the orthogonal laser light sheet. We used a camera frame rate of 2,100 frames/s, a shutter speed of 200 ms, and a lens aperture of 1.2 to capture images with a pixel resolution of 768 × 688. Both camera and motor were simultaneously controlled by a custom signal-generating Matlab program (Mathworks) via

We phase-averaged our velocity fields across nine wing strokes for Wing 1 and 10 wing strokes for each of Wings 2, 3, and 4, and computed a mean velocity vector for each phase. Wing deformation was equivalently measured in natural flight by spatially averaging all vectors in each phase-averaged field. Finally, we averaged these 84 phase vectors to produce a single velocity vector that represents the average flow of Washington approximately 5 days after eclosion, and magnitude and direction through our control region placed in a flight chamber (86 cm × 53 cm × 87 cm). Four synchronized high speed digital cameras (Phantom v5.1, Vision Research) mounted to a frame (80/20 Inc.) surrounding the infrared-illuminated chamber were used to film the nectarivorous moth hovering steadily in front of a freshly cut flower at 1,000 frames/s. We quantified wing deformation for five consecutive ventral stroke reversals (14 images each, as before), and also calculated the mean deformation and standard deviation of these five deformation stroke reversal of a robotically actuated fresh and stiff wing, and the natural deformations exhibited by a wing during hovering flight for comparison. A sample wing unit was extracted, prepared and mounted to the PIV motor assembly, as above, and subjected in both its fresh and dry states to the following treatment. Three synchronized high-speed digital cameras (Phantom v5.1, Vision Research) were used to film the oscillating wing from various directions at 1,000 frames/s. We used custom Matlab software (Hedrick 2008) to track and digitize an array of 12 points evenly distributed around the entire wing margin. The moth's natural wing pigmentation pattern provided landmarks that served as tracking points, and we used the same 12 tracking points for every deformation trial analyzed. We digitized the wing margin points through 14 consecutive video frame images (14 ms) encompassing each ventral stroke reversal. Five ventral stroke reversals were mapped and analyzed for each of the fresh and stiff wings.

2.6 Wing deformation measurements

We quantified the overall wing deformations at ventral stroke reversal of a robotically actuated fresh and stiff wing, and the natural deformations exhibited by a wing during hovering flight for comparison. A sample wing unit was extracted, prepared and mounted to the PIV motor assembly, as above, and subjected in both its fresh and dry states to the following treatment. Three synchronized high-speed digital cameras (Phantom v5.1, Vision Research) were used to film the oscillating wing from various directions at 1,000 frames/s. We used custom Matlab software (Hedrick 2008) to track and digitize an array of 12 points evenly distributed around the entire wing margin. The moth's natural wing pigmentation pattern provided landmarks that served as tracking points, and we used the same 12 tracking points for every deformation trial analyzed. We digitized the wing margin points through 14 consecutive video frame images (14 ms) encompassing each ventral stroke reversal. Five ventral stroke reversals were mapped and analyzed for each of the fresh and stiff wings.

wing, and the natural deformations exhibited by a wing during hovering flight for comparison. A sample wing unit was extracted, prepared and mounted to the PIV motor assembly, as above, and subjected in both its fresh and dry states to the following treatment. Three synchronized high-speed digital cameras (Phantom v5.1, Vision Research) were used to film the oscillating wing from various directions at 1,000 frames/s. We used custom Matlab software (Hedrick 2008) to track and digitize an array of 12 points evenly distributed around the entire wing margin. The moth's natural wing pigmentation pattern provided landmarks that served as tracking points, and we used the same 12 tracking points for every deformation trial analyzed. We digitized the wing margin points through 14 consecutive video frame images (14 ms) encompassing each ventral stroke reversal. Five ventral stroke reversals were mapped and analyzed for each of the fresh and stiff wings.

2.7 Principal components analysis

We performed a principal components analysis (PCA) on the wing trajectory of a moth during free flight hovering to determine its average stroke plane. We chose to use a PCA rather than a more commonly used linear regression method (Ellington 1984) because observations of wing position have variance in every spatial dimension. Thus, we avoid making an arbitrary choice for any particular dimension to be regressed upon another. The results of a PCA on a given data set are often similar to a linear regression, however, and they take the same form of mutually orthogonal eigenvectors (reported as principal components) and their associated eigenvalues.

Analyzing another multi-camera video sequence of the hovering flight with custom Matlab software (Hedrick 2008), we digitized two points on the rigid leading edge of the right forewing throughout five complete wing strokes: one point at the wing base and the other at 60% of the wingspan. A PCA on a two-dimensional lateral projection of this data set in global coordinates yielded two principal components. The principal component with the highest eigenvalue defines the dominant plane of motion swept out by the flapping wing, or the average stroke plane. This enabled us to rotate the coordinate system of our flow field data such that the stroke plane of our robotically actuated wing matched the moth's natural stroke plane.

The deformed surface of the wing was approximated at each time interval by linearly interpolating the 12 wing margin data points onto an intervening regularly spaced grid of 870 points. We then found an average best-fit plate of this data set in global coordinates yielded two principal components. The principal component with the highest eigenvalue defines the dominant plane of motion swept out by the flapping wing, or the average stroke plane. This enabled us to rotate the coordinate system of our flow field data such that the stroke plane of our robotically actuated wing matched the moth's natural stroke plane.

Thus, we distilled from surface coordinate data a single value for deformation that summarizes the detailed wing kinematics of each ventral stroke reversal. We calculated the mean deformation and standard deviation for our five fresh wing stroke reversals, and also for our five stiff wing stroke reversals.

3 Results

3.1 Principal components analysis

A PCA on a lateral view projection of the leading edge of wing deformation and captures nothing of the wing kinematics produced a first principal component of spatial or temporal details of the deformation pattern, $[-0.94 \ 0.33]$ with an eigenvalue of 0.40 and a second

principal component of $[-0.33 \pm 0.94]$ with an eigenvalue of 0.02. The first principal component describes the dominant plane of motion (the average stroke plane) and lies at 19° relative to the x-axis in global coordinates, within the range of stroke plane angles previously identified in hovering Manduca (Willmott and Ellington 1997). The stroke plane of our robotic wing was exactly vertical, so we applied a 71° counter-clockwise rotation to our robotic wing coordinate system after PIV analysis. All flow fields described hereafter account for this rotation into a biologically relevant configuration, and are therefore presented in the moth's global coordinates.

3.2 Flexural stiffness measurements

Overall flexural stiffness EI increased from the fresh wing state to the dry wing state for all three wings and these increases were significant, based on a Student's t -test performed on each data pair. Wing 1 EI increased from a mean of $9.79 \times 10^{-6} \text{ Nm}^2$ for the fresh wing to a mean of $2.04 \times 10^{-5} \text{ Nm}^2$ for the dry wing, $t = 6.29$, $P < 0.001$. Wing 2 EI increased from a mean of $2.84 \times 10^{-5} \text{ Nm}^2$ to $7.06 \times 10^{-5} \text{ Nm}^2$, $t = 13.68$, $P < 0.001$, and Wing 3 EI increased from a mean of $1.73 \times 10^{-5} \text{ Nm}^2$ to $3.45 \times 10^{-5} \text{ Nm}^2$, $t = 13.64$, $P < 0.001$. These data are consistent with those in prior studies; using a similar methodology, Combes and Daniel (2003) reported overall spanwise EI values for *M. sexta* in the range of 10^6 – 10^5 Nm^2 .

3.3 Wing deformation measurements

We computed a mean wing deformation value of 1.60 mm for fresh wing, with a standard deviation of 0.0544 mm . Our sample dry wing yielded a mean deformation of 1.15 mm , with a standard deviation of 0.0449 . By comparison, previous fresh wing state to the dry wing state. The vertical component of the fresh Wing 1 MAF was 17.9 cm/s , or 91% of its total magnitude. By comparison, the vertical component of the dry Wing 1 MAF was 1.5 cm/s , or 32% of its magnitude. The vertical component of the Wing 2 MAF changed from -40.6 cm/s at 91% magnitude for the fresh state to 1.3 cm/s at 8% magnitude for the dry state. The vertical component of the Wing 3 MAF changed from -48.4 cm/s at 98% magnitude for the fresh state to -7.3 cm/s at 40% magnitude for the dry state.

Our wing actuation method had fundamental limitations that prevented exact replication of a natural wing stroke.

First (as previously discussed), our motor had only one degree of active rotational freedom, versus three degrees of freedom on the moth. Second, in affixing the forewing and hindwing bases on a flat mounting plate, the degree of orientations more beneficial to lift than those produced by

actuation is actually diminished by the presence of passive elastic processes. Indeed prior work has established that torsional wing deformation is critical for flight in many insects, enabling the production of positive lift during both the upstroke and downstroke, despite having wings that are doubly hinged at the thorax (Wootton 1993; Ennos 1995).

3.4 Particle image velocimetry

All fresh wings produced flow fields with greater local velocities and more pronounced downward orientations throughout the stroke cycle than those of their stiff wing counterparts (Fig 5). The MAF for each fresh wing had a greater magnitude and a greater angle relative to the x-axis than the MAF for each dry wing (Fig 6). The MAF for Wing 1 decreased from a magnitude of 19.7 cm/s at -65° for the fresh state to 4.7 cm/s at 18° for the dry state. For Wing 2 the MAF decreased from 44.5 cm/s at -66° to 17.2 cm/s at 4° and for Wing 3 it decreased from 49.3 cm/s at -78° to 18.1 cm/s at -24° .

A hovering moth accelerates air downward, creating sufficient average vertical force to support its weight. Of particular interest, then, is the extent to which the vertical component of the MAF comprises the total MAF magnitude and how the vertical component changes from the fresh wing state to the dry wing state. The vertical component of the fresh Wing 1 MAF was 17.9 cm/s , or 91% of its total magnitude. By comparison, the vertical component of the dry Wing 1 MAF was 1.5 cm/s , or 32% of its magnitude. The vertical component of the Wing 2 MAF changed from -40.6 cm/s at 91% magnitude for the fresh state to 1.3 cm/s at 8% magnitude for the dry state. The vertical component of the Wing 3 MAF changed from -48.4 cm/s at 98% magnitude for the fresh state to -7.3 cm/s at 40% magnitude for the dry state.

4 Discussion

We found that flexible (fresh) wings produced mean convective flows with substantially greater magnitudes and orientations more beneficial to lift than those produced by

Fig. 4 A freshly extracted wing robotically flapped along a single axis of rotation approximates natural wing motion during hovering flight, illustrated in synchronized phases of a wing stroke at quarterly intervals. The collective tilt of the robotically actuated wing images is the result of a coordinate rotation to match the robotic wing stroke plane with the average stroke plane in hovering flight. The wings have been outlined to highlight their overall similarities in shape. The moth planform diagrams in the left column provide positional reference of the wing stroke phase relative to the viewpoint

stiff (dry) wings. We also showed that wing deformations possible by using high temporal resolution particle image velocimetry (2,100 frames/s) combined with real wings are similar to those measured in hovering flight, straddling flapped at natural wing beat frequency, rather than the naturally occurring values. These results were made dynamically scaled models. We are unaware of any other

Fig. 5 A robotically actuated fresh wing induces flows with greater overall velocities and more pronounced downward orientations than a dry wing, illustrated in phase-averaged velocity fields at synchronized quarterly wing stroke intervals for Wing 3. Arrow lengths and direction indicate magnitude and orientation of local fluid velocity, computed with PIV. Velocity magnitude is also represented in the pseudo-color background. The collective tilt of the control regions is the result of a coordinate rotation to match the robotic wing stroke plane with the average stroke plane in hovering flight. A cross-section of each wing appears in the third row of images, where the wing intersects the light sheet at ventral stroke reversal. A small gray region containing no data can be seen at the same location in every image, resulting from the combined affect of hardware and the PIV algorithm employed. The moth planform diagrams in the left column provide positional reference of the wing stroke phase relative to the laser light sheet and viewpoint

Flow visualization studies of animal locomotion using subsequent upstroke (Bergou et al. 2007, Willmott and Ellington 1997). We observed a more pronounced and significant pitch reversal—a torsional wave with greater

Passive wing deformation may lead to a number of amplitude-accompanying ventral stroke reversal in our aerodynamic mechanisms that may affect induced flow highly deforming fresh wings than in our lesser deforming and thus aerodynamic forces. For example, during supine wings. Wootton (1992) noted that, in general, the motion in natural flight a moth wing undergoes inertial-greater torsion an insect wing experiences on the upstroke, driven pitch reversal about a spanwise axis, manifest as the closer the aerodynamic force vector will approach the torsional wave that propagates from the tip to the base, vertical. He suggested that highly twistable wings that thereby establishing a positive angle of attack for the develop vertical force during both the downstroke and

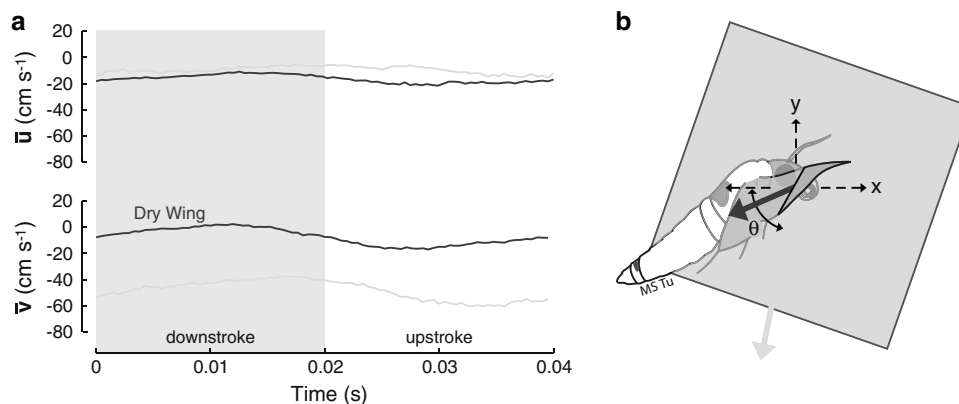


Fig. 6 Fresh wing mean flow velocities have greater magnitudes and both wing types, with \bar{u} representing the x-component and \bar{v} greater downward components than dry wing mean flow velocities, representing the y-component in global coordinates. a Each phase-averaged velocity field is blue dry wing, shown here for Wing 3a. b The stroke average of all phase-averaged velocity vectors is the MAF, plotted relative to the control region and a velocity vector per time step. The components of all such phase-averaged vectors are plotted for an entire phase-averaged stroke (wing)

upstroke permit slow, maneuverable flight, while less propagating from the leading to trailing edge of the wing twistable wings can only accommodate fast flight (Wootton could lead to a vertical force. To our knowledge, this 1992). Although Wootton addressed torsional consequence, mechanism has not been considered in studies of animal sequences during the translational stages of the wing stroke flight.

where we did not focus our attention, ventral stroke Spanwise bending was observed in both our robotically reversal by definition captures something of the end of the actuated wings and in natural flight. Investigations of downstroke and the beginning of the upstroke, and its fluid Manduca flight kinematics offer qualitative descriptions of dynamics are not independent of those manifest throughout spanwise wing bending and how it varies with different the stroke cycle. Our fresh wings with more pronounced flight modes and steering maneuvers (Weis-Fredrickson 1973 pitch reversals during supination presumably maintained Willmott and Ellington 1997). Few studies, however, have greater torsion throughout both the downstroke and upstroke than their dry wing counterparts, thereby contributing to the more vertically oriented MAF appearing at in our fresh wings than our dry wings, consistent with their stroke reversal.

The markedly greater pitch reversal in our fresh wings of deformation may be contributing to the induced flow may also generate greater circulation via the Kramer effect. Fields is unknown.

A bat, rigid wing undergoing rotation about a spanwise We relied upon a natural material stiffening process of axis while translating develops extra circulation proportional to the angular velocity of rotation, causing rotational forces that either augment or reduce the net force due to altered during flight, however, remain unknown. Here we translation (Sane 2003; Sane and Dickinson 2002). Wing rotation in advance of translational reversal augments translational forces, delayed rotation reduces them, and driven process, the pattern and extent of deformation likely rotation that is symmetrical about reversal has no net effect depend on overall wing trajectory, which is itself controlled (Sane and Dickinson 2002). The extent to which wing deformation contributes to the Kramer effect has not been explored. It is reasonable, however, to propose passive wing rigidity (Willmott and Ellington 1997). Although the chordwise bending waves may also contribute to the observed increase in wing rigidity (measured by torsion dynamic forces in much the same way as Pn waves and thus related to deformation in this study) may indeed contribute to thrust in fish (Combes and Daniel 2001; Wu 1971). At ventral stroke reversal, when the wing chord with flight speed, emergent deformation in this example is oriented vertically, a rapid, large amplitude wave may also be affected by other processes. For example, it

may be affected to some extent by the changes in external air flow that accompany changes in flight speed or by a change in the structural properties of the wing unit itself, resulting from the posterior shift in wingtip trajectory. If such a kinematic adjustment involved an increase in overlap between the forewing and hindwing, for example, the overall wing geometry would be modified and possibly the flexural stiffness distribution of the entire wing unit as well. Further, there is the possibility that flight muscles may have some degree of direct control of wing deformation, aside from the secondary effects associated with changes in wing trajectory. It is unclear how the flight muscles might achieve such a task, however.

Although stroke-to-stroke kinematic variations during steady hovering flight are smaller than those arising between different modes of flight (Willmott and Ellington 1997), one or more of the mechanisms proposed above might nevertheless be contributing to more subtle changes in wing deformation, possibly accounting for the variation measured in our free-flight analysis. The induced flow results presented in this study suggest that such changes in deformation may in turn affect important changes in the fluid dynamics and forces relevant to the flight of insects.

Acknowledgments The authors would like to thank Dr. Dana Dabiri (University of Washington) for his assistance with PIV methods, and two anonymous reviewers for providing helpful comments on this paper. This work was supported by DARPA and the Komen Endowed Chair to T.D., and a National Science Foundation Graduate Research Fellowship to A.M.

References

- Bergou A, Xu S, Wang Z (2007) Passive wing pitch reversal in insect flight. *J Fluid Mech* 591:321–337
- Biewener A, Dial K (1995) In-vivo strain in the humerus of pigeons (*Columba livia*) during flight. *J Morphol* 225:61–75
- Carruthers A, Thomas A, Taylor G (2007) Automatic aeroelastic devices in the wings of a steppe eagle *Aquila nipalensis*. *J Exp Biol* 210:4136–4149
- Combes SA, Daniel TL (2001) Shape, flapping and flexion: wing and pin design for forward flight. *J Exp Biol* 204:2073–2085
- Combes S, Daniel T (2003a) Flexural stiffness in insect wings I. Wing scaling and the influence of wing venation. *J Exp Biol* 206:2979–2987
- Combes S, Daniel T (2003b) Flexural stiffness in insect wings II. Spatial distribution and dynamic wing bending. *J Exp Biol* 206:2989–2997
- Combes S, Daniel T (2003c) Into thin air: contributions of aerodynamic and inertial-elastic forces to wing bending in the hawkmoth *Manduca sexta*. *J Exp Biol* 206:2999–3006
- Dickinson M, Gotz K (1996) The wake dynamics and flight forces of the fruit fly *Drosophila melanogaster*. *J Exp Biol* 199:2085–2104
- Ellington CP (1984) The aerodynamics of hovering insect flight. III. Kinematics. *Philos T R Soc B* 305:41–78
- Ellington CP (1995) Unsteady aerodynamics of insect flight. In: Ellington CP, Pedley TJ (eds) *Unsteady aerodynamics of insect flight*. The Company of Biologists, Cambridge, pp 109–129
- Ennos AR (1988) The inertial cause of wing rotation in Diptera. *J Exp Biol* 140:161–169
- Ennos AR (1995) Mechanical-behavior in torsion of insect wings, blades of grass and other cambered structures. *Proc Roy Soc Lond B Biol* 259:15–18
- Hedenstrom A, Johansson L, Wolf M, Von BR, Winter Y, Spedding G (2007) Bat flight generates complex aerodynamic tracks. *Science* 316:894–897
- Hedrick TL (2008) Software techniques for two- and three-dimensional kinematic measurements of biological and biomimetic systems. *Bioinspir Biomim* 3:034001
- Norberg R (1972) Evolution of flight in insects. *Zoologica Scripta* 1:247–250
- Sane SP (2003) The aerodynamics of insect flight. *J Exp Biol* 206:4191–4208
- Sane S, Dickinson M (2002) The aerodynamic effects of wing rotation and a revised quasi-steady model of flapping flight. *J Exp Biol* 205:1087–1096
- Sveen JK (2004) An introduction to MatPIV v. 1.6.1, Eprint No. 2, Department of Mathematics, University of Oslo. <http://www.math.uio.no/~jks/matpiv>
- Swartz S, Bennett M, Carrier D (1992) Wing bone stresses in free flying bats and the evolution of skeletal design for flight. *Nature* 359:726–729
- Weis-Fogh T (1973) Quick estimates of flight fitness in hovering animals, including novel mechanisms for lift production. *J Exp Biol* 59:169–230
- Willmott A, Ellington C (1997) The mechanics of flight in the hawkmoth *Manduca sexta*. I. Kinematics of hovering and forward flight. *J Exp Biol* 200:2705–2722
- Wootton RJ (1981) Support and deformability in insect wings. *J Zool* 193:447–468
- Wootton RJ (1992) Functional morphology of insect wings. *Annu Rev Entomol* 37:113–140
- Wootton RJ (1993) Leading-edge section and asymmetric twisting in the wings of flying butterflies (secta Papilionoidea). *J Exp Biol* 180:105–117
- Wootton RJ, Herbert RC, Young PG, Evans KE (2003) Approaches to the structural modelling of insect wings. *Philos T R Soc B* 358:1577–1587
- Wu TY (1971) Hydrodynamics of swimming propulsion. Part 1. Swimming of a two-dimensional flexible plate at variable forward speeds in an inviscid fluid. Part 2. Some optimum shape problems. Part 3. Swimming and optimum motions of slender fish with side fins. *J Fluid Mech* 46:337–355